By taking advantage of the fact that parallel streams of fluid flowing at low Reynolds number can maintain sharp boundaries (on the scale of micrometers) over distances of several centimeters, that reactions can be localized at the interfaces (fluid-capillary and fluid-fluid-capillary) with high spatial precision, and that reactive species present in these streams can be transported or generated with great versatility by using appropriate chemistries, FLO provides a method of microfabrication inside capillaries and other small enclosed spaces. With techniques developed for rapid prototyping of microstructures in polymers (*4*), it is straightforward to fabricate the network of capillaries that is required to bring together a range of solutions, in an appropriate order, to carry out multistep fabrication. Fluid flow can be controlled with whichever method seems most convenient for the application at hand (applied pressure, surface tension, gravity, or applied electrical potential). The liquid-liquid interfaces, and thus the features that are fabricated, can be positioned to within a few percent of the channel width by controlling the relative volumes of the different liquid streams entering the region in which reaction occurs. This procedure replaces the multiple stages of photolithography and pattern registration involved in photolithographic fabrication with a physical process—laminar flow—and permits the use of a wide range of chemistries in patterning.

FLO is probably most useful for making small numbers of systems for laboratory use and is not presently suited for high-volume manufacturing. The types of laminar flow patterns that are accessible limit the patterns that can be generated, but for certain applications—especially inside the channels used in electrochemical, microanalytical, and microsynthetic system—these patterns will allow the fabrication of a variety of useful structures.

References and Notes

1. M. Madou, *Fundamentals of Microfabrication* (CRC Press, New York, 1997).
2. O. Reynolds, *Philos. Trans.* **174**, 935 (1883); *ibid.* **186**, 123 (1895).
3. At a flow rate of 0.50 m/s, $Re = 50$ for aqueous phases in a 100-μm-wide channel. The broadening of a liquid-liquid interface by diffusion is given by $\langle x_{diff}^2 \rangle = 2Dt_{diff}$ with diffusion coefficient D (cm^2/s) and x_{diff} (cm) and t_{diff} (s) the distance and time of diffusion, respectively [P. W. Atkins, *Physical Chemistry* (Freeman, New York, 1994)]. The broadening of the features fabricated by FLO cannot be calculated with that equation alone because the profile of pressure-driven flow is parabolic [J. P. Brody, P. Yager, R. E. Goldstein, R. H. Austin, *Biophys. J.* **71**, 3430 (1996)]. The chemical reaction with the surface occurs in the stationary boundary layer; therefore the correct equation should account for lateral diffusion of the reagent within the layer, diffusional exchange with the moving liquid above the layer, and depletion of the reagent by the reaction. Preliminary experiments showed that broadening of an etched Au area increases roughly as the square root of the distance from the point where the separate flows join. The formula given above predicts a similar dependence, indicating that diffusional exchange between the boundary layer and the moving liquid dominates under our conditions.
4. D. C. Duffy, J. C. McDonald, O. J. A. Schueller, G. M. Whitesides, *Anal. Chem.* **70**, 4974 (1998).
5. We used pressure-driven flow generated with a syringe pump (Harvard Apparatus 22). Syringes were connected to the inlets of the microfluidic system by polyethylene tubing (Intramedic, inner diameter of 0.38 mm).
6. HE-300 solutions, Peacock Laboratories, 1901 South 54 Street, Philadelphia, PA 19143, USA. The counterion of the silver salt (X in the figures) is proprietary.
7. The roughness of the channel walls is typically 5 to 10 μm; the edge roughness of the etched or deposited structures is usually less than 1 μm.
8. Similarly, we deposited silver on one half of the inner surface of capillaries (PDMS, glass) by parallel laminar flow of water and an aqueous phase containing the premixed components of the electroless silver plating solution.
9. M. J. Cormier, D. M. Hercules, J. Lee, Eds., *Chemiluminescence and Bioluminescence* (Plenum, New York, 1973).
10. The use of laminar flow for "microfluidic diffusion-based separation and detection" has been described [B. H. Weigl and P. Yager, *Science* **283**, 346 (1999)].
11. H. A. Lowenstam and S. Weiner, *On Biomineralization* (Oxford Univ. Press, Oxford, 1989); S. Mann, J. Webb, R. J. P. Williams, Eds., *Biomineralization. Chemical and Biological Perspectives* (VCH, Weinheim, Germany, 1989).
12. J. Aizenberg, A. J. Black, G. M. Whitesides, *Nature* **394**, 868 (1998); J. Aizenberg, A. J. Black, G. M. Whitesides, *ibid.* **398**, 495 (1999).
13. D. Walsh, J. D. Hopwood, S. Mann, *Science* **264**, 1576 (1994); D. Walsh and S. Mann, *Chem. Mater.* **8**, 1944 (1996).
14. The Ag wire extended into the middle inlet as a result of back flow during the first few seconds of the deposition process.

15. This work was financially supported by the Defense Advanced Research Projects Agency and NSF grant ECS-9729405. Materials Research Science and Engineering Center–shared facilities supported by the NSF under grant DMR-9400396 were used. P.J.A.K. acknowledges the Netherlands Organization for Scientific Research (NWO) for a postdoctoral fellowship. We acknowledge W. Huck and Y. Lu for their help with the atomic force microscopy and scanning electron microscopy experiments.

9 February 1999; accepted 15 April 1999

Shock Melting of the Canyon Diablo Impactor: Constraints from Nickel-59 Contents and Numerical Modeling

C. Schnabel,[1] E. Pierazzo,[2]* S. Xue,[3] G. F. Herzog,[1]* J. Masarik,[4] R. G. Cresswell,[5] M. L. di Tada,[5] K. Liu,[5] L. K. Fifield[5]

Two main types of material survive from the Canyon Diablo impactor, which produced Meteor Crater in Arizona: iron meteorites, which did not melt during the impact; and spheroids, which did. Ultrasensitive measurements using accelerator mass spectrometry show that the meteorites contain about seven times as much nickel-59 as the spheroids. Lower average nickel-59 contents in the spheroids indicate that they typically came from 0.5 to 1 meter deeper in the impactor than did the meteorites. Numerical modeling for an impact velocity of 20 kilometers per second shows that a shell 1.5 to 2 meters thick, corresponding to 16 percent of the projectile volume, remained solid on the rear surface; that most of the projectile melted; and that little, if any, vaporized.

About 50,000 years ago, the impact of an iron meteoroid excavated Meteor Crater, Arizona (*1, 2*). During atmospheric entry and impact, some of the impactor remained solid, producing the Canyon Diablo meteorites. Most of the meteorites came from within 1.8 m of the preatmospheric surface of the impactor (*3, 4*). Another portion of the impactor melted (*5, 6*), producing the millimeter-size spheroids found in the soils around Meteor Crater (*7*). Nininger (*7*) estimated the total spheroid inventory to be 4000 to 7500 metric tons, or about 5% of the total mass of the Canyon Diablo meteoroid in space (*1, 8*). Here, we deduce the original depth in the impactor of the material that melted to form the spheroids and compare the result with the predictions of computer simulations of the Canyon Diablo impact. The results provide new information about what happens to medium-size meteoroids when they strike Earth or other solid objects in the solar system. The results also lend support to the evidentiary basis for applying theories of cratering dynamics to the

[1]Department of Chemistry, Rutgers University, Piscataway, NJ 08854, USA. [2]Lunar and Planetary Laboratory, University of Arizona, Tucson, AZ 87521, USA. [3]Graduate School of Oceanography, Narragansett Bay Campus, University of Rhode Island, Narragansett, RI 02882, USA. [4]Space Sciences Laboratory, University of California, Berkeley, CA 94720, USA. [5]Department of Nuclear Physics, Research School of Physical Sciences and Engineering, Australian National University, Canberra, ACT 0200, Australia.

*To whom correspondence should be addressed. E-mail: betty@lpl.arizona.edu; herzog@rutchem.rutgers.edu

larger impact events implicated, for example, in the formation of tektites and of some stratigraphic boundary layers.

To determine the original depth of the spheroids' precursor material in the meteoroid, we used measurements of a cosmogenic nuclide—a nuclide produced by cosmic rays while the meteoroid was in space. To a first approximation, the production of cosmogenic nuclides tends to be high near the surface of a large meteoroid and to decrease with increasing depth below the surface. Thus, lower measured concentrations of cosmogenic nuclides generally indicate greater preatmospheric depths. Not all cosmogenic nuclides in the spheroids, however, indicate depth equally well. Those with half-lives less than 10,000 years have decayed to undetectable levels. The volatile cosmogenic nuclides ^{3}He, ^{21}Ne, and ^{38}Ar may have been depleted when the spheroid precursor material melted. Loss of cosmogenic ^{26}Al and ^{10}Be (*9*) could have occurred as a consequence of oxidation during melting and the subsequent loss of Al_2O_3 and BeO (*5*).

The rarely measured nuclide ^{59}Ni (*10*) is, by contrast, well suited to be a depth indicator. The production of ^{59}Ni (half-life, 76,000 years) derives mostly (97 to 99%) from neutron capture by ^{58}Ni, with the rest due to nuclear reactions of protons and neutrons with the other isotopes of nickel. Thus, ^{59}Ni production depends almost exclusively on the concentration of just one element, Ni, in the meteoroid; conversely, the measured isotopic abundance of ^{59}Ni, ^{59}Ni/Ni, contains important information about the irradiation of the meteoroid in space. Because of the difficulty of changing isotopic ratios in ordinary physical and chemical processes, we expect the ^{59}Ni/Ni ratio to be conserved in the spheroids, except for radioactive decay. We determined the ^{59}Ni/Ni ratios in spheroids by accelerator mass spectrometry (*10*). An accelerating voltage of 14.2 MV was used and 213-MeV $^{59}Ni^{14+}$ ions were selected for analysis. A gas ionization detector provided unambiguous identification of individual ^{59}Ni ions, thereby permitting discrimination against the ^{59}Co isobaric interference. The ^{59}Ni/Ni ratios, corrected for radioactive decay from the time of impact, were then translated into preatmospheric depths of the precursor material through nuclear modeling calculations.

Canyon Diablo spheroids are described as having extraterrestrial, oxide-free cores (97.5% metal, 2.5% S and P) surrounded by a thin coating of metal oxide and terrestrial silicates (*5–7, 11*). We obtained four batches designated I, III, IV, and V, each comprising 500 to 2000 spheroids but differing with respect to average mass per spheroid (I, 1.08 mg; III, 6.6 mg; IV, 1.0 mg; V, 10 mg). Each sample analyzed for ^{59}Ni consisted of 40 to 100 mg of spheroids from one batch. In some cases we removed the oxide coatings by grinding and etching with HCl. To establish consistency of our ^{59}Ni measurements with published results, we analyzed metal-rich material from the Estherville mesosiderite, separated as described (*10*), as well as samples from four Canyon Diablo meteorites.

On average, the spheroids from Canyon Diablo contain one-sixth to one-seventh as much ^{59}Ni as the meteorites (Table 1). Nuclear modeling calculations of the ^{59}Ni activities produced by extraterrestrial neutron capture in a body similar to Canyon Diablo (*12*) indicate that as depth increases, the activities increase at first and then fall exponentially. The initial increase reflects the production of secondary neutrons by primary cosmic rays and thermalization of those neutrons through inelastic collisions. Capture by Fe and other processes attenuate the neutron flux at greater depths. The production of ^{59}Ni by neutron capture in the spheroids after they arrived at Earth's surface presents a possible complication. That production, however, is thought to be negligible: only 8.5×10^6 atoms per gram after 50,000 years of exposure, which corresponds to an activity of 0.15 disintegrations per minute per kilogram (dpm/kg) (*13*).

The calculated production rates of ^{59}Ni between the surface and 1.2 m depth in the meteoroid span the range of ^{59}Ni activities, 84 to 150 dpm/kg, of our Canyon Diablo meteorite samples at the time the meteoroid fell. The implied depths (0.1 to 0.8 m; Fig. 1) are similar to those inferred from other cosmogenic nuclides (*3, 4*).

The average ^{59}Ni activity of the spheroids, 13 ± 3 dpm/kg, is too low to have been produced near the preatmospheric surface of the meteoroid, where production rates would

Table 1. ^{59}Ni in the Estherville mesosiderite, Canyon Diablo meteorites, and Canyon Diablo spheroids. Measured ^{59}Ni/Ni ratios (10^{-12} atom/atom) have been normalized by reference to reactor-irradiated nickel with a ^{59}Ni/Ni ratio of 3.04 ($\pm$0.15) $\times$ 10^{-11} (*24*). For procedural blanks, an upper limit for the ^{59}Ni/Ni ratio of 0.05 $\times$ 10^{-12} has been determined. ^{59}Ni activities [disintegrations min^{-1} (kg meteorite)$^{-1}$] are calculated for the time of fall (50,000 years ago) for Canyon Diablo (*2*) and Ni contents of 7.1 weight % and 8.57 weight % for Canyon Diablo and Estherville, respectively (*25*).

Sample	^{59}Ni (counts)	^{59}Ni/Ni	^{59}Ni (activity)
	Estherville		
N3311	185	22.1 ± 1.6	
	480	22.1 ± 1.1	
N3311 (*10*)	905	23.6 ± 1.3	
Average			344 ± 12
	Canyon Diablo meteorites		
MPIH-3	124	4.2 ± 0.4	84 ± 7
MPIH-266	58	6.9 ± 1.1	138 ± 21
34.4340	314	7.7 ± 0.4	
	380	8.1 ± 0.6	
	368	7.3 ± 0.5	
	113	7.4 ± 0.7	
	216	7.1 ± 0.5	
Average		7.5 ± 0.4	150 ± 7
34.4367	95	3.3 ± 1.2	
	73	4.4 ± 0.6	
	111	4.8 ± 0.6	
Weighted average		4.4 ± 0.4	88 ± 8
Unnamed (*26*)		4.8 ± 1.2	95 ± 24
M-3 (*27*)		1.5 ± 0.6	30 ± 11
M-17 (*27*)		2.1 ± 0.4	41 ± 9
M-34 (*27*)		3.6 ± 0.5	73 ± 9
Average all			87 ± 15*
	Canyon Diablo spheroids†		
I-Q bulk	11	0.34 ± 0.17	
	31	0.39 ± 0.08	
I-R bulk	56	0.46 ± 0.08	
Weighted average		0.42 ± 0.05	8.3 ± 1.0
I-SIMC1 core	5	0.33 ± 0.14	
I-SIMC3 core	10	0.21 ± 0.07	
Average		0.27 ± 0.09	5.6 ± 1.5
III-3 core	44	0.49 ± 0.11	9.8 ± 2.0
IV-3 core	32	0.74 ± 0.12	14.7 ± 2.3
V-3 core	57	0.90 ± 0.12	18.0 ± 2.3
I-SC O bulk (*24*)	30	1.9 ± 0.4	24 ± 5
I-SC P bulk (*24*)	74	0.71 ± 0.14	8.9 ± 1.6
Average all			13 ± 3*

*1σ mean. †Spheroid sample names include the batch from which they came (I, III, IV, or V), a processing tag, and the designation bulk or core to indicate whether oxides were removed by HCl etching.

have exceeded 30 dpm/kg. We conclude that most spheroids did not form when atmospheric resistance to the incoming meteoroid melted surface material and blew molten droplets away. The average spheroid activity probably reflects the mixing of material from different depths. One possibility is that the spheroids represent well-mixed material from a continuous range of depths. The 1σ range of activities from 7 to 19 dpm/kg (~2σ of mean) implies depths between about 1.3 and 1.6 m, although individual spheroids within each sample may have come from other parts of the projectile.

Hydrocode simulations provide some information on the angular coordinates of the spheroids' parent material in the impactor and on other aspects of the impact discussed below. We modeled the projectile as a spherical iron object, 15 m in radius, impacting vertically into quartzite basement overlain by 80 m of limestone, an approximation of the stratigraphy at Meteor Crater (*1*). Neither size nor impact velocity is well defined for the Canyon Diablo meteoroid. Our choices of a radius of 15 m and an impact velocity of 20 km s^{-1} correspond to an average of several estimates (*1, 8*). To explore the range of common asteroidal impact velocities, we also carried out a simulation at an impact velocity of 15 km s^{-1} (*14*). The axially symmetric simulations were carried out using the two-dimensional finite difference hydrocode CSQ (*15*) coupled to the ANEOS equation-of-state package (*16*). A spatial resolution of 30 cells per projectile radius, equivalent to cells 0.5 m by 0.5 m in size, was used. One hundred Lagrangian tracer particles were regularly distributed in the projectile to follow its thermodynamic history (*17*).

The final state of matter in impact events is governed by the thermodynamics of shock compression and release and is described by the ANEOS equation of state. Shock compression is a thermodynamically irreversible process represented by the Hugoniot curve (the locus of unique states to which a material can be shocked from a given initial state). The decompression of matter can be approximated as an isentropic process. Shock pressures required for melting and vaporization are given by the intersection of the Hugoniot curve with the corresponding melting and vaporization isentropes (*18*). Values of melting shock pressures for Fe have been determined experimentally [242 GPa for incipient melting and 281 GPa for complete melting (*19*)] and theoretically (310 GPa and 389 GPa, respectively, using ANEOS). However, the Canyon Diablo impactor also contained ~7 weight % Ni. Although Ni should lower the melting point of Fe, shock experiments on stainless steel (~70% Fe, 20% Cr, and 10% Ni) indicate only a minor depression of the melting shock pressure of Fe: 234 GPa for incipient melting and 271 GPa for complete melting (*20*). With these values and an impact velocity of 20 km s^{-1}, we estimate that a shell 1.5 to 2 m thick and constituting ~15% of the mass remains solid (Fig. 2). The shell covers the trailing hemisphere and about one-third of the leading hemisphere. For an assumed impact velocity of 15 km s^{-1}, the solid shell thickens to ~5 m and constitutes ~63% of the mass. For both impact velocities, the rest of the projectile melts but does not vaporize because the peak shock pressures do not reach the threshold for incipient vaporization, ~800 GPa. Higher impact velocities would favor vaporization but would be atypical for Earth-crossing asteroids (*14*).

Although the impact modeling calculations for an impact velocity of 20 km s^{-1} show that ~80% of the Fe projectile melted, the estimated mass of Canyon Diablo spheroids, 4000 to 7500 metric tons (*7*), accounts for less than 10% of the assumed meteoroid mass, ~100,000 metric tons. We infer that the missing molten impactor material became too finely dispersed to recover during the expansion of shocked, volatile-rich target material (limestone) upon release from high pressure (*21*).

We suggest that the trailing hemisphere of the projectile is the likely location for the precursor material of the spheroids. Material in the leading hemisphere of the projectile would more readily mix with and be lost in a large volume of target rock (*22*). The ^{59}Ni measurements imply that the liquid precursor material for the spheroids came from depths of 1.3 to 1.6 m beneath the preatmospheric surface of the impactor. These depths are consistent with calculations of the shallowest depths at which liquid forms for an impact velocity of 20 km s^{-1} but not of 15 km s^{-1}. We suggest further that Canyon Diablo "sluglets"—rare, oddly shaped objects that may have undergone partial melting (*7*)—have come from average depths intermediate between those of the meteorites and of the spheroids (Fig. 2).

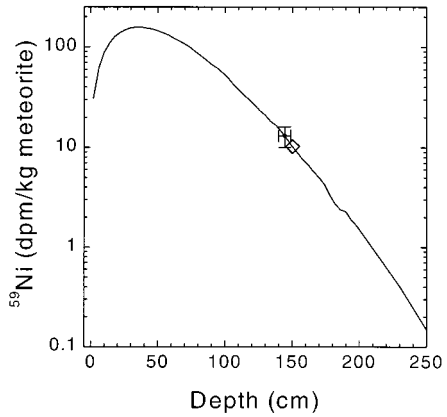

Fig. 1. Calculated ^{59}Ni production rates (curve). The data point represents the average ^{59}Ni activity in Canyon Diablo spheroids at the time of fall (Table 1); the diamond shows the average calculated activity for the entire meteoroid (*28*).

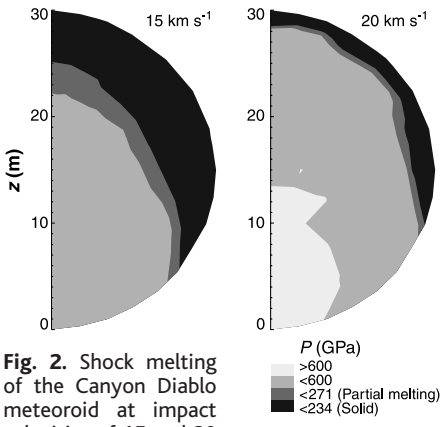

Fig. 2. Shock melting of the Canyon Diablo meteoroid at impact velocities of 15 and 20 km s^{-1}, as modeled with the two-dimensional hydrocode CSQ. Complete melting occurs at shock pressures above 271 GPa. The western (not shown) and eastern hemispheres are axially symmetric.

References and Notes

1. E. M. Shoemaker, in *The Moon, Meteorites and Comets. The Solar System. Vol. 4*, B. M. Middlehurst and G. P. Kuiper, Eds. (Univ. of Chicago Press, Chicago, 1963), pp. 301–336; in *Structure of the Earth's Crust and Deformation of Rocks* (Rept. 18, International Geological Congress, XXI Section, Copenhagen, 1960), pp. 418–434.
2. K. Nishiizumi *et al*., *Geochim. Cosmochim. Acta* **55**, 2699 (1991); F. M. Phillips *et al*., *ibid.*, p. 2695; S. R. Sutton, *J. Geophys. Res.* **90**, 3690 (1985).
3. D. Heymann, M. E. Lipschutz., B. Nielson, E. Anders, *J. Geophys. Res.* **71**, 619 (1966).
4. E. S. Michlovich *et al*., *ibid.* **99**, 23187 (1994).
5. W. R. Kelly, E. Holdsworth, C. B. Moore, *Geochim. Cosmochim. Acta* **38**, 533 (1974). Relative to Canyon Diablo meteorites, the metallic portions of Canyon Diablo spheroids contain more Ni, whereas the oxidized portions contain less Ni. Mass balance calculations indicate a net depletion of iron from the spheroids, which Kelly *et al*. attributed to the loss of iron-rich oxides, mainly during the flight of the spheroids away from the site of the impact. Be and Al oxidize more readily than Fe. We expect their oxides to follow iron oxides and to undergo similar loss processes.
6. P. J. Blau, H. J. Axon, J. I. Goldstein, *J. Geophys. Res.* **78**, 363 (1973).
7. H. H. Nininger, *Arizona's Meteorite Crater* (World, Denver, CO, 1956), pp. 81–114.
8. D. J. Roddy, *Proceedings of the 9th Lunar and Planetary Science Conference* (Pergamon, New York, 1978), pp. 3891–3930; J. B. Bryant *et al*., *ibid*., pp. 3931–3964; D. J. Roddy *et al*., *Proceedings of the 11th Lunar and Planetary Science Conference* (Pergamon, New York, 1980), pp. 2275–2308; R. M. Schmidt, *ibid*., pp. 2099–2128.
9. S. Xue *et al*., *Meteoritics* **30**, 303 (1995).
10. M. Paul *et al*., *Nucl. Instrum. Methods* **B83**, 275 (1993).
11. C. W. Mead, J. Littler, E. C. T. Chao, *Am. Mineral.* **50**, 667 (1965).
12. Calculations are based on the Los Alamos High Energy Transport Code System (LCS), a system of Monte Carlo computer codes that treats cosmic ray particle production and transport. We model the Canyon Diablo meteoroid as a sphere 15 m in radius with the average composition of Canyon Diablo meteorites (*5*) irradiated by 10^5 galactic cosmic ray (GCR) protons

at a rate of 4.8 protons cm^{-2} s^{-1}—that is, the GCR primary particle spectrum averaged over a typical solar cycle. The production rate of ^{59}Ni was calculated by integration over the energy of the product of neutron fluxes, computed by LCS, and neutron-capture cross sections weighted by target nuclei concentration. Statistical uncertainties of 2 to 3% are associated with the numbers of particles simulated; overall uncertainties of ~15% allow for the uncertainties of the cross sections and primary GCR flux. The calculations depend weakly on radius in this size region and should describe, within the uncertainties, ^{59}Ni production in bodies with radii from 13 to 17 m (*23*) [J. Masarik and R. C. Reedy, *Geochim. Cosmochim. Acta* **58**, 5307 (1994); R. E. Prael and H. Lichtenstein, *Los Alamos Report LA-UR-89-3014I* (1989); J. F. Briesmeister, *Los Alamos Report LA-12625-M* (1993)].

13. The activity of terrestrially produced ^{59}Ni, A_{59}, in the spheroids is calculated to be 0.15 disintegrations per minute per kilogram from the relation

$$A_{59} = [1 - \exp(-\lambda_{59} t_{\text{terrestrial}})] \times {}^{58}Ni \int_{1 \times 10^{-8}\ \text{MeV}}^{20\ \text{MeV}} \Phi(E)\sigma(E)dE$$

where ^{58}Ni is the concentration of that isotope; $\Phi(E)$ is the flux of neutrons at energy E calculated by LCS (*12*) at the elevation of Meteor Crater, 1561 m (J. Masarik and J. Beer, *J. Geophys. Res.* **B104**, 12099 (1999); $\sigma(E)$ is the cross section for neutron capture by ^{58}Ni (*23*); λ_{59} is the decay constant for ^{59}Ni, 1.73×10^{-11} min^{-1}; the concentration of ^{58}Ni is based on an average total Ni content of ~16% in spheroids (*6*); and $t_{\text{terrestrial}}$ is the time of impact of the Canyon Diablo meteoroid, 0.05 million years ago (*1*).

14. A value of 15 km s^{-1} corresponds to the median impact speed and a value of 20 km s^{-1} to the average impact speed for known Earth-crossing asteroids [C. F. Chyba, *Icarus* **92**, 217 (1991); ———, T. C. Owen, W.-H. Ip, in *Hazards Due to Comets and Asteroids*, T. Gerhels, Ed. (Univ. of Arizona Press, Tucson, 1994), pp. 9–58; D. L. Rabinowitz, E. Bowell, E. M. Shoemaker, K. Muinonen, *ibid*., pp. 285–312].
15. S. L. Thompson, *Tech. Rep. SAND77-1339* (Sandia National Laboratory, Albuquerque, NM, 1979).
16. ——— and H. S. Lauson, *Tech. Rep. SC-RR-710714* (Sandia National Laboratory, Albuquerque, NM, 1972).
17. E. Pierazzo, A. M. Vickery, H. J. Melosh, *Icarus* **127**, 408 (1997).
18. H. J. Melosh, *Impact Cratering* (Oxford, New York, 1989).
19. J. D. Bass, B. Svendsen, T. J. Ahrens, in *High-Pressure Research in Mineral Physics,* M. H. Manghnani and Y. Syono, Eds. (Terra Scientific, Tokyo/American Geophysical Union, Washington, DC, 1987), pp. 393–402.
20. J. D. Bass, T. J. Ahrens, J. R. Abelson, T. Hua, *J. Geophys. Res.* **95**, 21767 (1990).
21. The process of target decompression but not of meteoroid dispersal is described by S. W. Kieffer and C. H. Simonds [*Rev. Geophys. Space Phys.* **18**, 143 (1980)].
22. E. Pierazzo, D. A. Kring, H. J. Melosh, *J. Geophys. Res.* **103**, 28607 (1998); E. Pierazzo and H. J. Melosh, *Earth Planet. Sci. Lett.* **165**, 163 (1999).
23. Cross Section Evaluation Working Group, *Report BNL-NCS-44945* (*ENDF-102*) (Brookhaven National Laboratory, Upton, NY 1995).
24. J. Klein *et al*., *Lunar Planet. Sci.* **XXVI**, 763 (1995).
25. To place all the Canyon Diablo ^{59}Ni contents, whether measured in meteorites or in spheroids, on a consistent scale, we converted ^{59}Ni/Ni ratios to ^{59}Ni activities in an object with the average Ni content, 7.1 weight %, of Canyon Diablo meteorites [C. B. Moore, J. Littler, D. Nava, in *Meteorite Research,* P. M. Millman, Ed. (Springer-Verlag, New York, 1969), pp. 738–748; B. Mason and E. Jarosewich, *Mineral. Mag.* **39**, 204 (1973)]. This Ni content was also used in the nuclear modeling calculations. In addition, iron and nickel contents were measured by direct current atomic emission spectrometry (DC-AES) and inductively coupled plasma mass spectrometry (ICP-MS), respectively, yielding the following values (weight %): MPIH-3: Fe 92.3, Ni 6.6; MPIH-266: Fe 92.5, Ni 6.2; 34.4340: Fe 93.8, Ni 6.6; 34.4367: Fe 91.8, Ni 6.5; III-3: Fe 75.1, Ni 14.0; IV-3: Fe 82.1, Ni 14.1; V-3: Fe 78.3, Ni 18.4. Relative uncertainties are 5% for both elements.
26. M. Honda and J. R. Arnold, *Handb. Phys.* **46**, 613 (1967).
27. J. H. Kaye, in *Nuclear Chemistry Research at Carnegie Institute of Technology, 1961–1962* [Progress Report for U.S. Atomic Energy Commission Contract AT(30-1)-844, 1962], pp. 43–46.
28. The nuclear modeling calculations extend only to a depth of 2 m. Wiggles in the curve reflect statistical limitations set by the number of particles followed through the calculation. We used a polynomial fit to extrapolate the production rates to depths greater than 2 m. The data points have been placed on the curve at the depths inferred from the modeling calculations.
29. We thank R. Clarke Jr. for sample N3311; T. Kirsten for Canyon Diablo samples MPIH-3 and MPIH-266; M. E. Lipschutz for Canyon Diablo samples 34.4340 and 34.4367; C. Moore for spheroids; and J. Klein, A. Hildebrand, and two anonymous referees for helpful contributions to this work. Supported in part by NASA grants NAG5-4327 and NAGW-5159 and U.S. Department of Energy contract DE-FG03-96ER14676.

1 March 1999; accepted 3 June 1999

Atomic-Scale Quasi-Particle Scattering Resonances in $Bi_2Sr_2CaCu_2O_{8+\delta}$

E. W. Hudson,[1] S. H. Pan,[1]* A. K. Gupta,[2] K.-W. Ng,[2] J. C. Davis[1]†

Low-temperature scanning tunneling spectroscopy of the high transition temperature (high-T_c) cuprate $Bi_2Sr_2CaCu_2O_{8+\delta}$ reveals the existence of large numbers of identical regions with diameters of about 3 nanometers that have a relatively high density of low-energy quasi-particle states. Their spatial and spectroscopic characteristics are consistent with theories of strong quasi-particle scattering from atomic-scale impurities in a *d*-wave superconductor. These characteristics include breaking of local particle-hole symmetry, a diameter near twice the superconducting coherence length, and an inverse square dependence of their local density-of-states on distance from the scattering center. In addition to the validation of *d*-wave quasi-particle scattering theories, these observations identify a source for the anomalously high levels of low-energy quasi-particles in $Bi_2Sr_2CaCu_2O_{8+\delta}$ at low temperatures.

Impurity atoms and atomic-scale defects, even in very small concentrations, can strongly influence the properties of materials. This is of great practical significance in semiconductor technology, for example, where the conductivity of pure semiconductors can be increased many orders of magnitude by doping with a few parts per million of specific impurities. Another example is the doping of small numbers of Ti atoms into sapphire to create the optical conditions necessary for high-power, tunable lasers.

Impurities also play a critical role in superconductivity. Conventional superconductors, such as Nb and Pb, are highly sensitive to the presence of magnetic impurity atoms (*1*), which suppress the critical temperature by breaking Cooper pairs through spin-flip scattering (*2*). Nonmagnetic impurities, on the other hand, have little effect on conventional superconductors. In the high-T_c superconductors, however, doping even with nonmagnetic impurities can cause dramatic effects. In fact, it is hole doping in the form of additional oxygen atoms that turns the cuprate oxides from antiferromagnetic insulators into high-T_c superconductors. However, impurity doping with Zn or Ni is known to reduce the critical temperature, modify the energy gap, increase the residual resistivity, and alter the vortex phase diagram (*3–5*).

Despite many important effects of impurity atoms on the macroscopic properties of high-T_c superconductors (*6*) and despite numerous proposals for scanning tunneling microscopy (STM) study of impurity quasi-particle scattering in these systems (*7–11*), no direct observation and systematic study of the effects of quasi-particle scattering at the atomic scale have been reported. Theory indicates that quasi-particle scattering at impurities can reveal information about the symmetry of the order parameter, the momentum dependence of the energy gap, and the microscopic mechanism of superconductivity (*8, 12*). Several studies predict that impurity atoms create quasi-particle scattering resonances that have characteristic signatures both in the spatial shape of the quasi-particle cloud near the scattering center and in their tunneling spectrum (*7–12*). Furthermore, it has also been

[1]Department of Physics, University of California, Berkeley, CA, 94720–7300, USA. [2]Department of Physics and Astronomy, University of Kentucky, Lexington, KY 40506–0055, USA.

*Present address: Department of Physics, Boston University, Boston, MA, 02215, USA.

†To whom correspondence should be addressed. E-mail: jcdavis@socrates.berkeley.edu